

Hydrodynamic simulations of molecular outflows driven by slow-precessing protostellar jets

Michael D. Smith ¹ & Alexander Rosen ²†

¹Armagh Observatory, College Hill, Armagh BT61 9DG, Northern Ireland

²Dublin City University, School of Mathematics, Glasnevin, Dublin 9

Accepted Received ; in original form

ABSTRACT

We present hydrodynamic simulations of molecular outflows driven by jets with a long period of precession, motivated by observations of arc-like features and S-symmetry in outflows associated with young stars. We simulate images of not only H₂ vibrational and CO rotational emission lines, but also of atomic emission. The density cross section displays a jaw-like cavity, independent of precession rate. In molecular hydrogen, however, we find ordered chains of bow shocks and meandering streamers which contrast with the chaotic structure produced by jets in rapid precession. A feature particularly dominant in atomic emission is a stagnant point in the flow that remains near the inlet and alters shape and brightness as the jet skims by. Under the present conditions, slow jet precession yields a relatively high fraction of mass accelerated to high speeds, as also attested to in simulated CO line profiles. Many outflow structures, characterised by HH 222 (continuous ribbon), HH 240 (asymmetric chains of bow shocks) and RNO 43N (protruding cavities), are probably related to the slow precession model.

Key words: hydrodynamics – shock waves – ISM: clouds – ISM: jets and outflows – ISM: molecules

1 INTRODUCTION

Collimated outflows are integrally connected with star formation (Richer et al. 2000; Reipurth & Bally 2001). The outflowing mass is distributed over a large volume and can far exceed the suspected mass of the growing star. This suggests that momentum is generated deep within the potential well of the young star and that, after extraction, is transmitted into the ambient gas. Jets of molecules are often associated with the youngest protostars. However, one view suggests that these jets are highly ballistic and that the low density of the surroundings does not efficiently soak up the jet momentum. As the protostars age and the accretion rate declines, their molecular jets become less dense and more atomic which may increase the efficiency. Alternatively, the jet thrust might be sprayed into a large volume through precession of the direction of release. The consequences of such a scenario are explored here.

Observations of protostellar jets frequently provide evidence for precession. Some examples with precession an-

gles in the range 5° – 20° are Cep A (Gueth & Guilloteau 1999); Cep E (Eisloffel et al. 1996); HH 31 (Gomez et al. 1997); HH 34 (Bally & Devine 1994); and HH 333 (Arce & Goodman 2001). Larger precession angles are suggested for L 1228 (Bally et al. 1995), PV Cep (Gomez et al. 1997) and IRAS 20126+4104 (Shepherd et al. 2000).

We present here a sequence of three dimensional hydrodynamic simulations. They were executed with a modified version of ZEUS-3D which solves a detailed cooling function and a reduced chemical network (see § 2). We drive a molecular jet into a uniform molecular environment. Previously, we have examined the physical and observational structure which results for jets with (i) a range of densities relative to the ambient density (Rosen & Smith 2004b), (ii) significant sustained changes to the inlet mass flux (Rosen & Smith 2003) and (iii) a range of precession angles but all with a fast precession period (Rosen & Smith 2004a). Fast jet precession, however, does not produce the S-symmetry as observed in the above examples. Instead, the jet impact describes an expanding ring which fragments into a multitude of shocks. In addition, a stagnation region appears once the impact no longer encounters the precession axis, as exam-

* E-mail: mds@arm.ac.uk

† E-mail: alex.rosen@dcu.ie

ined by Lim (2001) for an atomic model. The ambient gas trapped in this region may lead to observable features.

Here, we investigate the consequences of jets undergoing slow precession, the precession speed being defined in terms of the appropriate dynamical time (see §2). We wish to identify the global structures associated with a range of commonly observed emission lines. Curved outflows of various types are indeed observed. The very young protostar VLA 1623 is associated with a slender tube-like CO outflow which meanders through the ρ Ophiuchi cloud Dent et al. (1995). A few bipolar outflows show C-type or mirror symmetry rather than S-type or point symmetry (e.g. the S233IR outflow, Beuther et al. 2002). Such flows could result from twin jets associated with one protostar within a close binary: the space velocities of both jets at each instant are the vector additions of fixed components in the protostar's frame and the variable orbital velocity (Frank et al. 1998; Masciadri & Raga 2002). There are even some theories that tie the precession of jets to the warping of the disk (Lai 2003). The star formation process, which must be able to generate a large number of binaries, thus includes potential mechanisms for varying the direction of ejection.

Besides identifying outflow properties, there are two issues we try to resolve. Firstly, strong H_2 1–0 S(1) emission is often measured in the near-infrared at $2.12\ \mu m$. Taking this to be ten percent of the total H_2 emission, which is taken to be ten per cent of the total radiation, then the jet power must be at least 100 times stronger. This can just be reconciled with current theories for young, Class 0 protostars which may drive jets of high power in comparison to their bolometric luminosity. However, taking near-infrared extinction into account as well as the fact that ballistic jets tend to be inefficient radiators, the jet powers become uncomfortably high.

Another motivating measure concerns the distribution of outflowing mass with radial velocity. All of our previous three-dimensional simulations predict shallow distributions: a high fraction of gas is accelerated to high speed. In contrast, there are numerous outflows for which steep relationships are deduced from CO line profiles. We summarise these measurements of the slope in the mass-velocity and intensity distributions in § 5.1. We test here if these problems with the efficiency and velocity distribution might both be solved by slowing the rate of precession.

The simulations are executed with a modified version of ZEUS-3D (Smith & Rosen 2003) which tracks the molecular fraction, calculates a quite detailed cooling function, and includes molecular dissociation and reformation. The cooling and chemistry are solved implicitly. Details and tests have been presented by Smith & Rosen (2003) and Rosen & Smith (2004b).

2 ZEUS-3D WITH MOLECULAR COOLING AND CHEMISTRY

2.1 Hydrocode properties

We have modified the ZEUS-3D code, which usually updates variables with an explicit scheme, to include a semi-implicit method to calculate the time-dependent molecular and atomic hydrogen fractions. We have added a limited

Table 1. Major parameters altered between the simulations discussed (upper set) and the initial/boundary values for the ambient medium and jet (lower list) which were not varied.

Run	P10	Q10	R10
Precession period	50	400	400
Precession angle	10°	10°	10°
Pulsation period	60	60	60
Pulse amplitude	30%	30%	0.01%
Jet speed (axis)		$100\ km\ s^{-1}$	
Jet speed (perimeter)		$70\ km\ s^{-1}$	
Jet density		$2.32\ 10^{-19}\ gm\ cm^{-3}$	
Jet temperature		100 K	
Jet radius		$1.7\ 10^{15}\ cm$	
Ambient density		$2.32\ 10^{-20}\ gm\ cm^{-3}$	
Ambient temperature		10 K	
$n(H_2)/n_H$		0.5	
Init. specific heat ratio		1.4286	

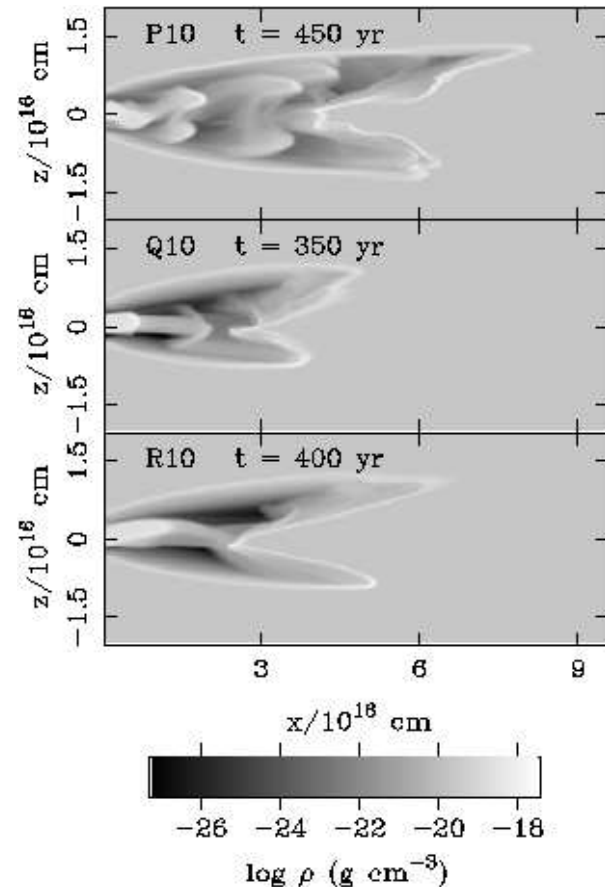


Figure 1. Midplane cross sections of density. Each cross section is scaled to the same maximum and minimum and the scale is displayed below the cross sections. The complete computational domain in the two axes is displayed. The vertical axis is the z -axis in each panel.

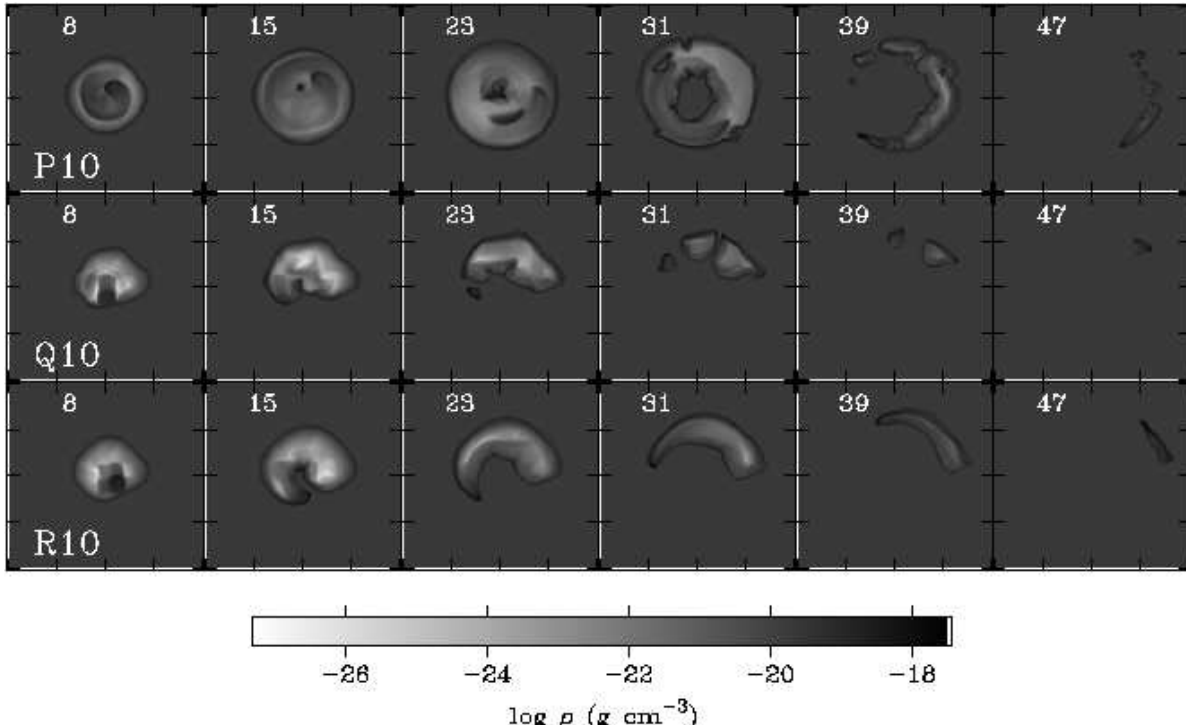


Figure 2. Axial cross sections of density for simulations P10 (top row), Q10 (middle row) and R10 (bottom row). Each row of snapshots is taken from the time that is displayed in the corresponding panel in Fig. 1. The axial position in R_j is given in the upper left of each panel. Each cross section is scaled to the same maximum and minimum and the scale is displayed below the cross sections. The complete computational domain in the two axes is displayed. The distance between adjacent tick marks is 1×10^{16} cm. The vertical axis is the y -axis and the horizontal axis is the z -axis, and so the view is from the jet inlet boundary looking down the x -axis (i.e., toward the $+x$ -direction).

equilibrium C and O chemistry to calculate the CO, OH and H₂O abundances. Equilibrium CO and H₂O is a reasonable estimate at high density, consistent with the low spatial resolution of the cooling layers behind shock waves (Rosen & Smith 2004b). The details of the many components of the cooling function and the limited chemistry network are discussed in the appendices of Smith & Rosen (2003). In summary, we include cooling through rotational and vibrational transitions of H₂, CO, and H₂O, H₂ dissociative cooling and reformation heating, gas-grain cooling/heating, and a time-independent atomic cooling function that includes non-equilibrium effects. We assume that the gas includes an additional 10% by number of helium atoms, so the mean atomic mass is 2.32×10^{-24} g. The dust temperature is fixed at 20 K.

The cooling and chemistry are poorly resolved as a result of the demands placed by the need for three dimensional simulations. The problem is located within the radiative cooling zones behind shock waves. Since fast shocks with speed exceeding ~ 25 km s⁻¹ dissociate molecules, both atomic and molecular cooling zones arise in the present simulations. In fast shocks, the atomic cooling length is considerably shorter than the molecular cooling length and so provides the most stringent scale to resolve. However, this length is of the order of just $10^{13} - 10^{14}$ cm, given the initial range in density. Therefore, we make no attempt to resolve the atomic cooling zone and note that peak temperature

obtained in the simulations will be considerably less than the physical values associated with the shock speed. Fortunately, as utilised in previous studies (Stone & Norman 1993; Suttner et al. 1997), shock conservation laws are accurately maintained despite the lack of resolution. This is used to argue that the dynamics are correctly predicted although the atomic emission line fluxes are incorrect (the images of total atomic cooling presented here should be considered as providing only the general locations of shocked atomic gas).

The molecular cooling zones are significantly longer: $\sim 10^{20}/n$ cm. While shocks into the lower-density ambient gas are resolved, those in the jet are generally not. Hence, we restrict our predictions to the properties of the global outflow rather than individual shocks. This is particularly relevant to the chemistry. By choosing equilibrium H₂O and CO chemistry, the influence of the cooling zone on the entire flow is minimised. However, a non-equilibrium treatment of H₂ is necessary and, unless care is taken, this could lead to misleading results. Tests carried out by us at various levels have shown that the resolution achieved here is adequate to describe the global properties but that much more detailed fine structure will appear at higher resolution (Suttner et al. 1997; Pavlovski et al. 2002). Other potential causes of inaccuracy were discussed by Rosen & Smith (2003, 2004b).

2.2 Chosen simulations

In a previous work, we described a simulation of a molecular jet with a precession angle of 10° and a fast precession rate, which we designated P10. In this paper, we discuss P10 and two additional simulations with a 10° precession angle, but with a much slower precession rate (see Table 1). One simulation is identical to P10 save for the precession rate, and is designated here as Q10. The other simulation is identical to Q10 with the exception of the amplitude of the jet pulsation, which is reduced from $\pm 30\%$ to $\pm 0.01\%$ (essentially a constant initial jet velocity). We designate this simulation R10.

We modify the jet velocity in P10 and Q10 with a 30% pulsation and a 60 year period (see Table 1). In addition, all simulations have a radial shear that reduces the jet velocity at the jet edge to $0.7 v_j$. The precession period is 50 yr in P10, but 400 yr in Q10 and R10. The former is relatively slow compared to the dynamical time $R_j/v_j = 5.4$ yr, but fast relative to the flow evolution time of order 500 yr (see below). The slower rate is of the same order as the flow evolution and also our x -axis crossing time.

We define the precession rate as fast if it rotates faster than the outflow expands. Then, the jet contributes to advancing an entire annulus into the ambient medium, generating a ring structure or annulus of fixed width (twice the jet radius). To calculate the expansion time, we first note that the density of the precessing jet decreases to $\sim \rho_j/(1+(D \sin \theta)/r_j)$ at a distance D along the x axis. This is effectively a one-dimensional expansion since the width of the annulus remains constant as its distance from the axis about which the jet is precessing increases. Momentum balance with the external medium of uniform density ρ_a then yields

$$\rho_a U^2 \sim \frac{\rho_j}{1+(D \sin \theta)/r_j} (v_j - U)^2 \quad (1)$$

on equating the ram pressures, where U is the average advance speed of the fast precessing jet into the ambient medium. If we now consider the expansion to be braked when U is reduced, say, to $0.5 v_j$, then the expansion time, $t_E = D/U$, is given by

$$t_E = \frac{\rho_j - \rho_a}{\rho_a} \frac{2r_j}{v_j \sin \theta}. \quad (2)$$

If the precession is slow then we expect a meandering stream to have time to develop, rather than a ring. For the parameters chosen here, $t_E = 559$ yr. Therefore, our chosen ‘slow’ precession rate still displays the effects due to precession whereas a ‘gradual’ precession, with a period far exceeding t_E would approximate to a non-precessing structure.

The computational volume is simulated with a uniform staggered grid divided into zones each of which spans 2×10^{14} cm in each direction. For all three of the 10° precession simulations, we use a grid of $480 \times 205 \times 205$ zones. Since the jets have large precession angles, the eventual time-averaged momentum axis for the flow (here, the x -axis) is never the jet flow direction. The initial jet radius, R_j , is 1.7×10^{15} cm and is therefore resolved by 8.5 zones. The boundary zones satisfy outflow conditions with the exception of the zones on the inner x -boundary that allow jet inflow.

We assume conditions that we suspect are relevant to Class 0 protostellar jets. In all cases, the jet is initialised with a hydrogenic nucleon density of 10^5 cm^{-3} . We set the jet-to-ambient density ratio to 10, the initial jet temperature to 100 K and the ratio of jet-to-ambient thermal pressure to 100. The nominal, mean axial jet speed is $v_j = 100 \text{ km s}^{-1}$. This yields an initial Mach number with respect to (the uniform) ambient medium of 140.

3 PHYSICAL PROPERTIES

3.1 Internal structure

Midplane slices of density are displayed in Fig. 1 at a simulation stage where side projections of the outflows almost spanned the entire computational grid. In fact, at the times shown in Fig. 1, both Q10 and R10 have jet material as far from the inlet as $x \sim 8.5 \times 10^{16}$ cm ($50 R_j$). Most striking is the existence of a jaw-shaped structure in the slow precessing cases Q10 and R10 as well as the fast precessing case. Also, slow precession generally yields lower density cavities (darker in Fig. 1) since swept up material is not quickly replaced by the jet. The midplane density slices reveal the shocks from the pulsing in Q10, and relative smoothness of the non-pulsed flow in R10.

We display the cross-sectional structure normal to the jet axis for the same three simulations in Fig. 2. For P10, this shows a complete annulus mid-way down the jet which fragments near the leading edge. For Q10 and R10, the slow precessing results in a helical flow pattern from $+z$ (the right side of each panel) to $-z$ through $+y$ (the top of each panel) and back again through $-y$. This is consistent with the time-variation of the precession at the origin. A comparison between the Q10 and R10 jets reveals that the instability seen in the ‘islands’ of jet material at large x are primarily caused by the pulsing. Specifically, the islands seen in Q10 at $x/R_j = 31$ and 39 are unified into an arc-like bow structure in R10. However, as presented below, the integrated H_2 emission portends future fragmentation in the R10 flow.

Quite high transverse velocities are encountered in the slow precessing cases. A plot of velocity vectors and density contours (Fig. 3) for R10 shows that outward facing velocity vectors are associated with the helical bow shock far from the inlet. Closer to the inlet (in the first couple of panels), the precessing jet is evident. In addition, there is a large transverse velocity ($\sim 50 \text{ km s}^{-1}$) in the third panel, where the bow shock has nearly spun around on itself.

3.2 Speed and size

We have previously analysed the fast precessing jet simulations to determine their capability of producing giant outflows of size $\sim 1 \text{ pc}$ (Rosen & Smith 2004a). We employed a model to fit the mean speed of advance and to determine the effective drag coefficient corresponding to the aerodynamic properties and atmospheric resistance. This term, C_d , can also be parameterised as a change in area across the bow shock in the usual ram pressure approximation for the Mach disk advance speed, as used in § 2. We deduced low values of C_d in the range 0.18–0.27 for a range of density ratios and

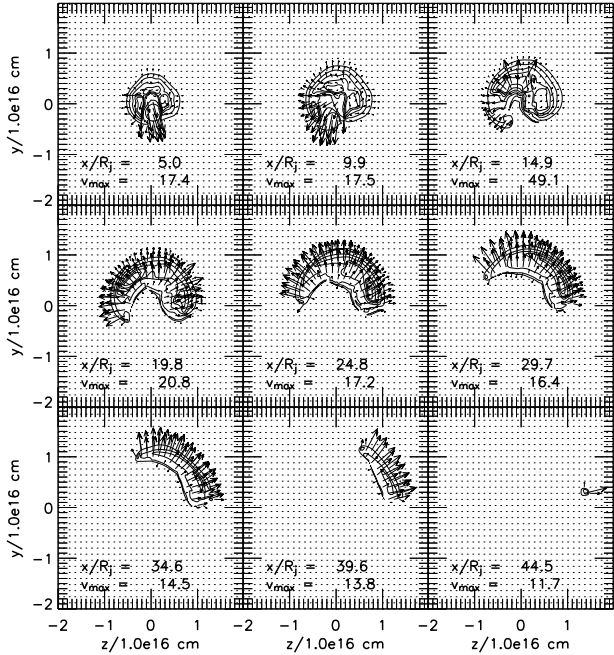


Figure 3. Transverse velocity vectors and mass density contours in simulation R10 at $t = 350$ yr. The value labelled x is the axial position and v_{max} is the maximum transverse velocity in the panel (in km s^{-1}). The velocity vectors are displayed for every sixth zone and the maximum vector length in any panel is normalised to the maximum velocity in that panel. Density contours are at $\log \rho = -24.0, -23.0, -22.0, -21.0, -20.0, -19.0$, and -18.0 .

mass fluxes whereas we expect a value of unity if the ram pressure of the jet is modified by its expansion only.

For the fast precessing cases, the drag coefficient increases with precessing angle, from 0.20 for 5° half-precession angle to 0.45 for the 20° case. Within this model, we found that the fast precessing jets could reach a distance of 1 pc between 35,000 and 85,000 yr, showing evidence for deceleration despite the small drag coefficients. We concluded that outflows reach large sizes in times comparable to the Class 0 protostellar stage.

Here, the evolutions of the linear extents are shown in Fig. 4. Also shown are the best fit models and integrated times to 1 pc. We find that the drag coefficient varies according to the physical structure. The advancing bow shocks of run Q10 result in a low drag coefficient of 0.22. In contrast, the continuous ribbon produced by run R10 leads to the highest drag (0.45). This is consistent with expectations from fluid dynamics since the 3D aerodynamic bow shapes permit fluid to flow easily past the obstacles, whereas the ribbon presents a more obtrusive object. The time required to reach 1 pc according to the extrapolated model remains within the 40,000–60,000 yr range.

4 SIMULATED MOLECULAR LINE EMISSION

4.1 Integrated line emission

We estimate the associated radiated energy rate for a few molecular and atomic emission lines using the zonal values

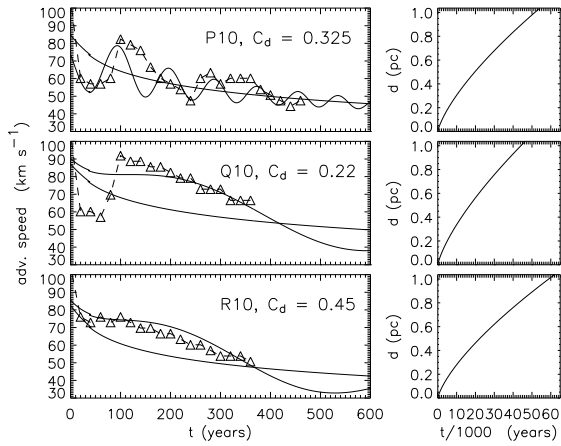


Figure 4. Advance speed and estimated time to 1 pc for precessing molecular jets. The panels on the left show the time-averaged (over 20 years) advance speed of the bow shock, which are indicated by the triangles connected with the dashed line. The advance speeds have been fitted with a model that includes the momentum drag from the interaction of the jet with the ambient medium (Rosen & Smith 2004a). The inferred drag coefficient, C_d , is listed in the upper right of these panels. The models are indicated by the solid lines, the most accurate includes the slowly-damped sinusoidal variation caused by the precession while the monotonically decreasing fit assumes that the jet momentum is evenly spread in the advancing disc/annulus. The panels on the right show the time required to reach 1 pc, according to the extrapolation of the advance speed.

for mass density, temperature and molecular fraction. We integrate the emission for selected molecular lines at specific times with the assumption that the outflow and foreground cloud are optically thin; examples of these integrations are shown in Figs. 5–11. The H_2 line emission is based on a non-LTE approximation to the vibrational populations (Draine et al. 1983) and the CO rotational emission is calculated according to McKee et al. (1982). The only plot presented for run P10 (Fig. 5), which was discussed previously, includes new integrations in “atomic” emission as well as in molecular hydrogen emission for comparison.

The atomic emission is derived from the cooling function used in the code (based on Sutherland & Dopita 1993), unmodified to select a specific emission line. As with all of these integrations, they provide a guide to the location and extent of emission and relative brightness of regions of the flow rather than accurate predictions. In run P10, the brightest atomic emission is spatially correlated with relatively bright regions of molecular hydrogen emission, a result that is not surprising since both are related to the cooling of post-shock material. However, the brightest atomic emission occurs in localised small knots and filaments whereas the H_2 emission is relatively more diffuse.

The images of atomic emission prominently display inner cones associated with a stagnation point (the knot at 3×10^{16} cm and some of the emission forward of that). Also, there is no extended atomic emission from the leading edge of the jet, where there is significant H_2 emission. This suggests that the atomic emission is produced in strong

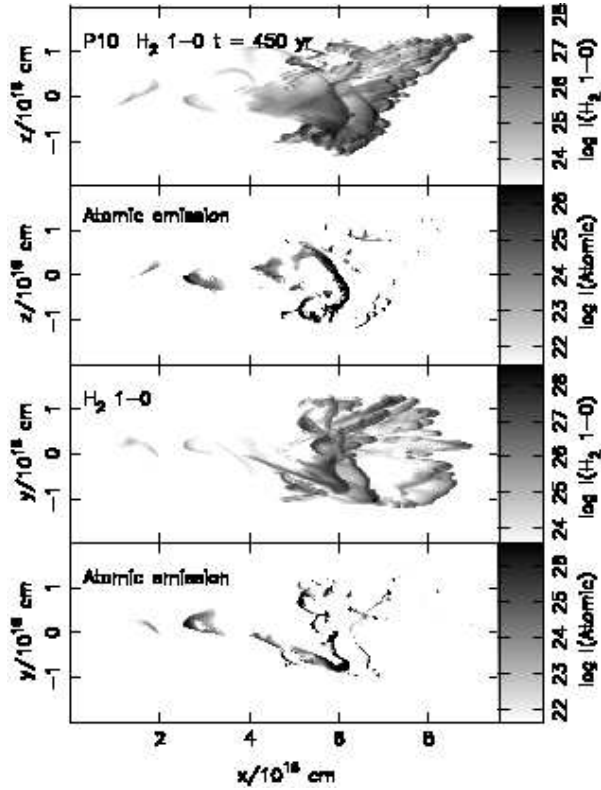


Figure 5. Two orthogonal views of simulation P10 at $t = 450$ yr in one molecular emission line and one general ‘‘atomic’’ emission line. In the top two panels, the integration is along the y -axis, and in the bottom two, integration is along the z -axis. In order to produce a more complete picture of atomic emission, the image has been rescaled so that the maximum luminosity in the appropriate panels is 3 orders of magnitude lower than the actual maximum luminosity (which is very localised). The luminosities are in erg s^{-1} from bins with roughly the same size as the 3D zones used in the simulations (i.e. $2 \times 10^{14} \text{ cm}$).

shocks directly associated with the jet impact rather than the predominantly weak oblique shocks associated with the advancing aerodynamic bow-shaped features.

The simulated images of molecular hydrogen and atomic emission reveal the shock structure. In simulation Q10 (Figs. 6 and 7), the pulsing jet at the inlet leads to many internal shocks, while in R10 (Figs. 8 and 9) the constant speed yields a shock in the form of a single sinuous ribbon.

This ribbon contains an apparent ‘‘x’’ at $x \sim 2.5 \times 10^{16} \text{ cm}$ in the y -integrated images (Fig. 8). It is most prominent in the atomic emission from simulation R10 but is also bright in all emission lines shown. While more difficult to perceive, a similar feature is also distinguishable in the plots for run Q10. In the images generated by z -integration (Fig. 9), this ‘‘x’’ is a more complicated structure, suggestive of a disk of emitting material seen edge-on. Such a disk is confirmed by viewing the jet from various angles about the mean momentum (x) axis, which we display in Fig. 10. Moreover, this disk can be seen in the second panel of the R10 density cross sections in Fig. 2 and contours of the third panel in Fig. 3.

From these images, we hypothesise that the ‘‘x’’ is re-

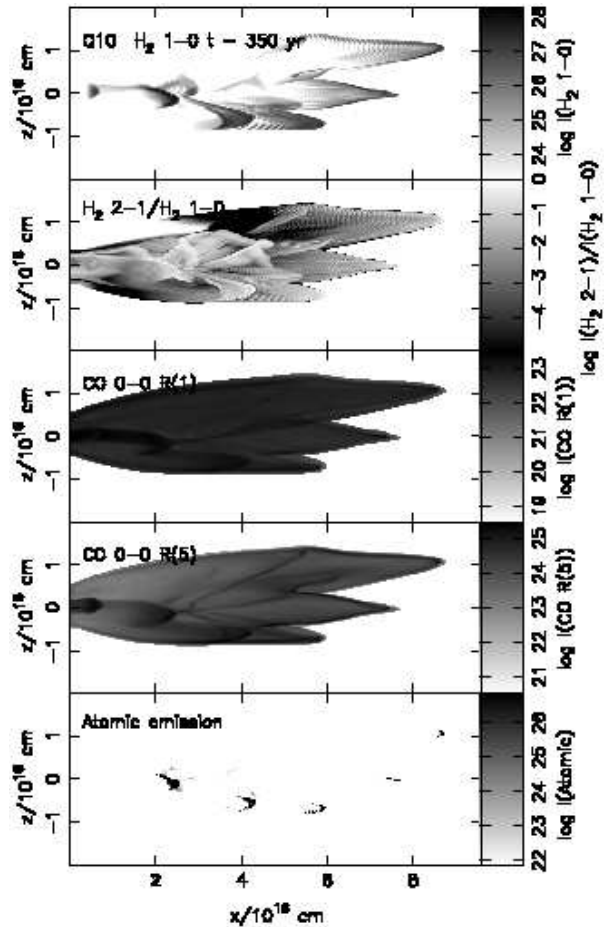


Figure 6. Integrated emission along the y -axis in simulation Q10 at $t = 350$ yr for four molecular emission lines and one general atomic emission line. Further details are as in Fig. 5.

lated to a stagnation disk that at the time of this image is being squeezed from both sides, since the precession rate is just sufficient for more than a half-turn to exist at this x -position. In addition, the third panel in the velocity vector plot has a very large maximum transverse velocity ($\sim 50 \text{ km s}^{-1}$ compared with 17.5 km s^{-1} transverse velocity from the nominal jet speed and the input angle). It seems plausible that this large velocity is caused by the release of accumulated material from this stagnation disk. To investigate further, we have also executed isothermal simulations of a fast dense jet which show evidence for large tangential velocities near the jet-crossing point.

The ‘‘x’’ in atomic emission appears similar to that in the HH222 (seen in a plate of the HH34 superjet complex, Bally & Devine 1994), although the the process responsible is likely different in the real source, which is many times the size of what has been simulated here.

We present the temporal variation of molecular hydrogen emission from run Q10 in Fig. 11. As opposed to the fast precessing cases, where at early times we saw an elliptical ring form, here we see a strong asymmetry about the mean momentum axis. However, at early times this axis may not be obvious. Additionally, the bow shocks evolve in a compli-

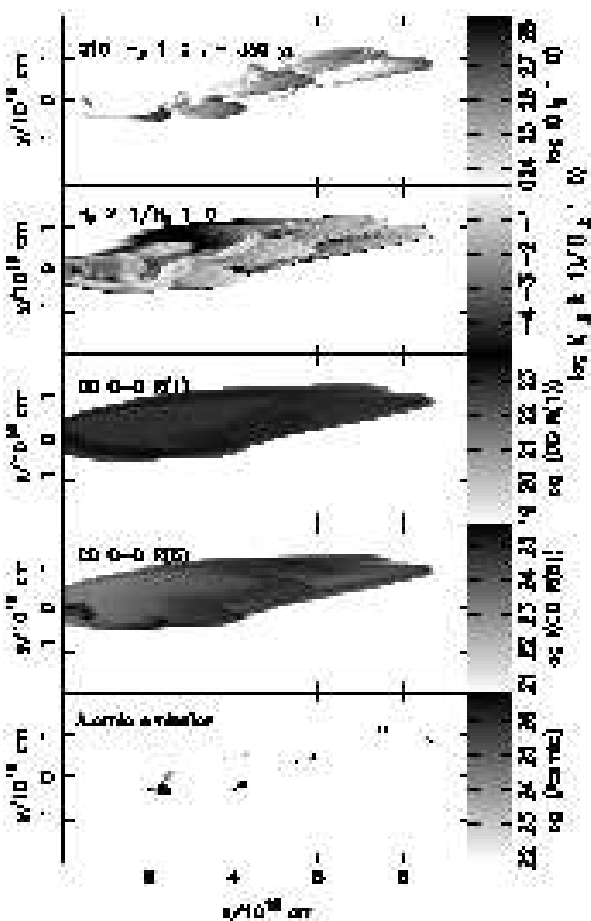


Figure 7. Integrated emission along the z -axis from simulation Q10 at $t = 350$ yr in four molecular emission lines and one general atomic emission line. Further details are as in Fig. 5.

cated and fascinating fashion, with the strongest emission moving forward through the bow as the entire emitting region moves forward. For times just after $t = 300$ yr, there is a rapid change in the direction of the jet, which could be (mis-)interpreted as a dramatic event at the jet origin. Of course, in this case we know that only a smooth variation is responsible. The sequence of bow shocks at late times bears a striking similarity with L1634 (O'Connell et al. 2004), which is an order of magnitude larger than our simulations.

The vibrational excitation is measured by the H_2 2-1/1-0 line ratio. The excitation distributions reveal the most intense shocks, and its brightest regions generally coincide with bright regions of the 1-0 line itself. Noteworthy is that the region associated with the “x” feature in R10 has quite a high H_2 line ratio.

The moving CO emission displays an outline of the dense jet plus swept-up ambient material. The CO emission lines, particularly the 0-0 R(1), emphasise the sinusoidal projection of the helical flow pattern. The ribbon is traced back to the source. Note that the individual advancing bow shocks in run Q10 sweep out separate protruding CO cavities (Fig. 6). Finally, the CO R(5) images (i.e. in the rotational emission line with a frequency of 691 GHz, from

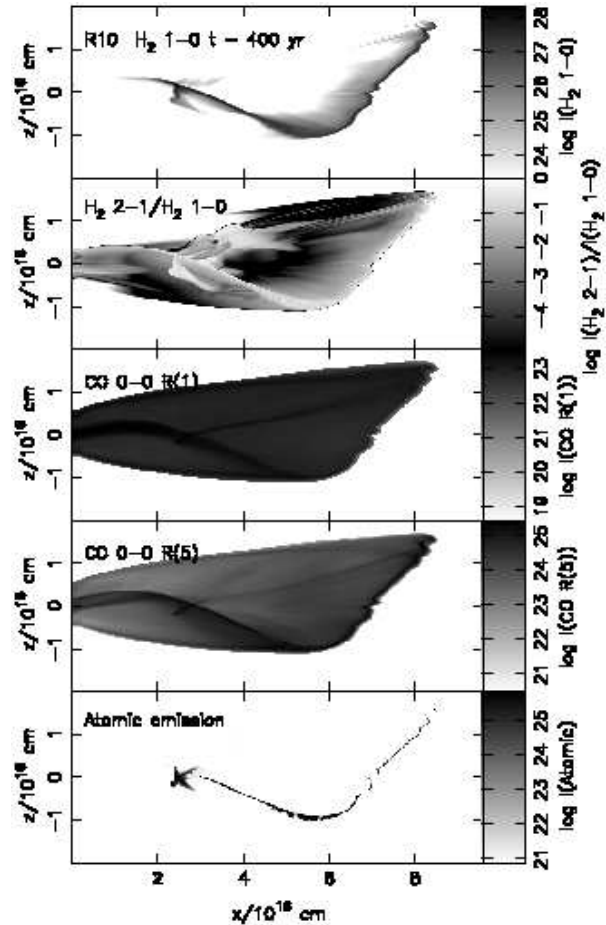


Figure 8. Integrated emission along y -axis from simulation R10 at $t = 400$ yr in four molecular emission lines and one atomic emission line. Further details are as in Fig. 5.

116 K above the ground state) again appear somewhere between the H_2 emission and the CO R(1), as expected. Both the cavity structure and internal bullets are evident.

4.2 Total line emission and efficiency

The evolution of the total molecular line emission from molecular outflows is of relevance to the global modelling of star formation (e.g., the Unification Scheme, Smith 2000; Stanke 2000; and Yu et al. 2000). In contrast with previous pulsating and some of the fast precessing simulations, the total molecular intensities for molecular hydrogen and CO monotonically increase over time for the new simulations presented here. They cover the same range as run P10 (see Fig. 10 in Rosen & Smith 2004a). The non-pulsing case R10 increases in the most smooth fashion of the three simulations discussed here. The periods of flat or decreasing luminosity that exist in Q10 coincide with the appearance of a new knot near the inlet. Eventually this knot brightens sufficiently that the total flux increases.

We have also calculated the ratio of the total emission compared to a time-averaged kinetic energy flux (mechanical power) from the jet source for a sample of our molecular jet

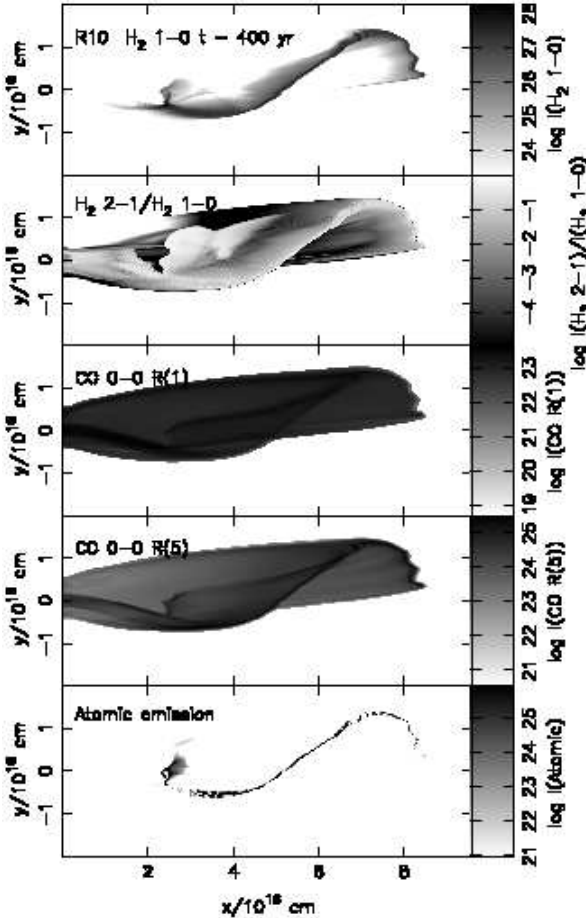


Figure 9. Integrated emission along z -axis from simulation R10 at $t = 400$ yr in four molecular emission lines and one atomic emission line. Further details are as in Fig. 5.

simulations (see Fig. 11 from Rosen & Smith 2004a). Typically, the H_2 1-0 emission line had an efficiency of around 0.1–1.0% of the mean mechanical energy, with an increase in this range over the lifetime of the simulation. For CO the range varied from 10^{-7} at early times to roughly 10^{-5} at late times ($t \sim 500$ yr), with a more monotonic variation with time between the two extrema than in the H_2 case. We have also computed the evolution of these ratios for the two new simulations and find values close to that of Simulation P10. In general, both the variation over time in the mechanical power and in the H_2 to mechanical power ratio (by 0.2 dex, usually) is smaller in the slow precessing cases than in P10. Also, the ratio is typically smaller (0.1 dex) in the pulsed case (Q10) than non-pulsed case (R10). For the CO ratio, Q10 is smaller or equal to the ratio in P10, and the R10 CO ratio is typically larger or equal to that of P10, but over time both asymptotically approach the evolution of P10.

We have also calculated the the instantaneous radiative loss from each part of our cooling function at 50 yr intervals for the new simulations. These losses are then compared with the time-averaged mechanical luminosity (power) input at the inlet up to the point in time that the losses are computed. We find that at $t = 350$ yr, the total losses are roughly 30% of the mean power, with two-thirds of that being from

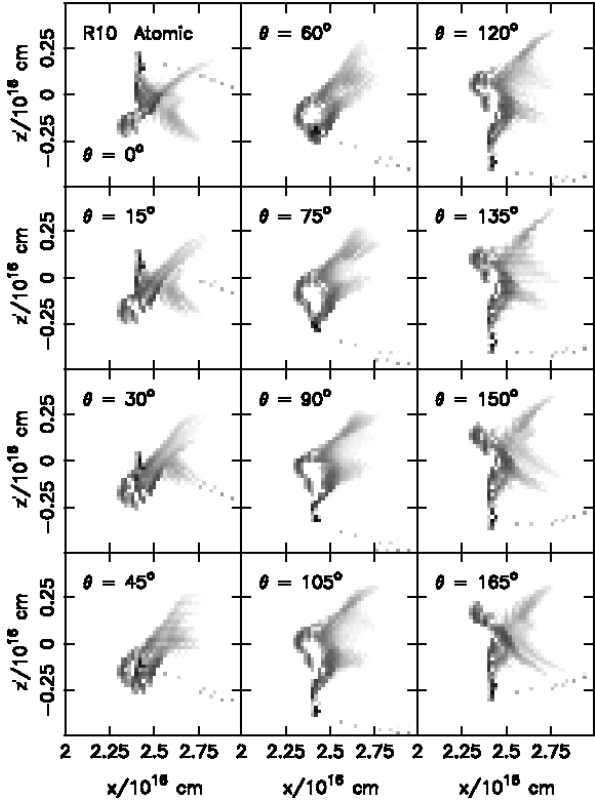


Figure 10. Close-up rotation of views about the axis in simulation R10. By rotating about the jet axis of the “x” feature in Fig. 8, we see a more varied appearance.

a combination of H_2 ro-vibrational and atomic cooling. For the pulsed case (Q10), the atomic emission alone is about 5% of the mean power at this time, but for the non-pulsed case (R10), it’s fraction is only 0.5%. This is explained by the many internal bow shocks, which are sites of heating and dissociation for the initially molecular gas. The evolution of the H_2 1-0 S(1) emission efficiency from 0.1% to 1% in these simulations is associated with a nearly constant 4% ratio of emission from this line to the total H_2 ro-vibrational cooling rate.

Other major contributors to the cooling function include (values in parentheses are the fractions of each cooling component of the mean power for the jet near the end of the simulation): H_2 dissociation (2–3%), H_2O rotational transitions due to collisions with H and H_2 (~ 5%), and CO rotational transitions due to collisions with H and H_2 (2%). The individual component ratios of luminosity to mean jet power nearly always increase monotonically with time, as does the total, which increases by about 5% of the mean power in every 50 yr interval.

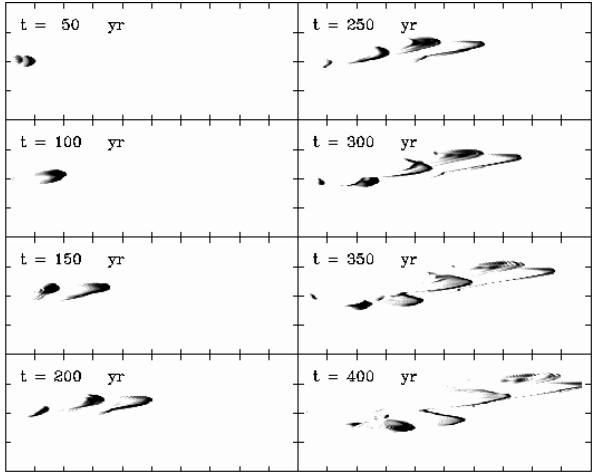


Figure 11. Evolution of the 1-0 S(1) molecular hydrogen emission for simulation Q10. Integrations of H₂ 1-0 emission along the z -axis (the y -axis is the vertical dimension in all the panels).

5 VELOCITY DISTRIBUTION OF MASS AND MOLECULAR LINE EMISSION

5.1 Background

There have been many recent measurements of the slope in the mass-velocity distributions, interpreted from CO line profile data of protostellar outflows. Once the slow turbulent motions of nearby molecular clouds are meticulously subtracted (e.g., Yu et al. 2000), there is frequently a quite shallow distribution (with γ in $dm/dv \propto v^{-\gamma}$ occasionally as low as 1) at low radial velocities. A steeper slope ($\gtrsim 6$) is found at higher velocities, where the turnover occurs at $v_{break} \sim 10 \text{ km s}^{-1}$. Note, however, that the majority of powerful outflows may possess very steep profiles even at low speeds (Davis et al. 1998; Ridge & Moore 2001). Many of these outflows possess low collimation, suggesting that the wide outflow sweeps up a high mass to low speeds.

Additionally, a similar analysis has been performed for H₂ line profiles of some protostellar outflows (Salas & Cruz-González 2002). The equivalent γ is defined as $\gamma_m = dL(1 - 0 S(1))/dv \propto v^{-\gamma_m}$. The authors measure a range of γ_m between 1.8 and 2.6 above a break velocity which lies between 2 – 17 km s⁻¹ (the flux is flat or slightly rising below this radial velocity). We wish to test here if jets undergoing wide-angle long-period precession could decelerate sufficiently to match the observations of large γ_m at high speeds.

Previous simulations of ballistic jets with small precession angles yielded quite shallow values for the CO γ of 1.2–1.6 (Smith et al. 1997) or even shallower (0.9–1.3, Rosen & Smith 2004b). Non-ballistic jets, with equal or lower density than the ambient medium, also generated outflows with low γ values (Rosen & Smith 2004b). The fast precessing jets in Rosen & Smith (2004a) yielded a somewhat larger range of slopes for the small velocity region, (0.4–1.6). The higher γ values are associated with combinations of the following conditions: jets viewed near the plane of the sky, jets with a large precession angle, or jets which are initially atomic.

The simulations in Rosen & Smith (2004b) possess flux-velocity distributions of H₂ that do not closely resemble the observations of Salas & Cruz-González (2002), with a strong increase in luminosity at small velocities. This is not disturbing since the 1-0 S(1) emission properties are very sensitive to the physics within the radiative shocks. In hydrodynamic shocks, the molecules radiate efficiently only after being strongly accelerated and compressed. This suggests that the shock viscosity is instead provided by ambipolar diffusion in the molecular sections.

Axisymmetric simulations similar to those in Downes & Ray (1999) were analysed by Downes & Cabrit (2003). They obtained a low-velocity CO γ of 1.5, which is in the range of commonly observed values. This may have been the result of smaller jet densities and longer time coverage than we have used. Indeed, Smith et al. (1997) also found that the γ value increases with time in 3D simulations. Downes & Cabrit (2003) also attempt to reproduce the H₂ results of Salas & Cruz-González (2002), with some success but use an approximation (LTE) that is more appropriate for densities larger than in most of their flow.

5.2 Mass- and intensity-velocity relations

We have performed a similar analysis for the velocity distributions of mass, CO R(1) luminosity and H₂ 1-0 luminosity for each of the simulations presented here. Power law slopes γ , γ_{CO} and γ_{H2} are determined. We list the results for a sample of viewing angles, defined as the angle of the x -axis out of the plane of the sky toward the observer, in Table 2. We also display the data for one viewing angle (15°) in Fig. 12. Note that both red and blue shifted line wings are displayed in this figure. A summary of our results follows.

- The precession period has a small influence on the mass distribution as measured by the power-law index γ . For viewing angles $> 15^\circ$, there is a slightly steeper slope in the mass relation in the slow-period precessing cases, which have slopes that are fairly close to each other (the non-pulsed case marginally increases the slope).
- For the CO distribution, there is a stronger and opposite dependence of γ_{CO} on the precession rate, with most viewing angles of the slow-precession cases yielding a slope 0.5 smaller than the rather shallow 1.2 for P10.
- In simulations of fast precessing jets, we found that the slopes for the CO distribution exceed those of the mass distribution, occasionally quite significantly. This is similar to a result from the low density jet simulations of Downes & Cabrit (2003). This trend extends to the slowly precessing molecular jet simulations presented here, although the differences between the two slopes are small in Q10 and R10 than in P10.
- At least for large viewing angles ($> 45^\circ$), we confirm previous results that there is an inverse relationship between γ and the viewing angle (Smith et al. 1997, Lee et al. 2001, Downes & Cabrit 2003, Rosen & Smith 2004b and Rosen & Smith 2004a).
- Additionally, we have examined the evolution of the velocity distributions for each of the molecular jet simulations at two different programme times. In contrast to the findings of Smith et al. (1997), we find that the slope of these

Table 2. Mass Spectra Power-Law Dependences

Sim.	t(yr)	type	θ	range of $\log v $	γ	N ^a	type	θ	range of $\log v $	γ	N ^a	
P10	450	mass	15	0.5–1.0/1.0–1.4	1.02/1.87	7/15	CO	15	0.5–1.0/1.2–1.4	1.20/1.96	7/9	
			30	0.5–1.0/1.1–1.7	0.52/1.68	7/37			30	0.5–1.0	1.22	7
			45	0.5–1.0/1.4–1.8	0.63/1.65	7/38			45	0.5–1.0	1.22	7
			60	0.5–1.0/1.4–1.9	0.57/1.45	7/54			60	0.5–1.0	1.21	7
			90	0.5–1.0/1.6–1.9	0.46/1.37	7/39			90	0.5–1.0	1.21	7
Q10	350	mass	15	0.5–1.0	0.26	7	CO	15	0.5–1.0	0.49	7	
			30	0.5–1.0	0.56	7			30	0.5–1.0	0.76	7
			45	0.5–1.0	0.63	7			45	0.5–1.0	0.80	7
			60	0.5–1.0	0.59	7			60	0.5–1.0	0.74	7
			90	0.5–1.0	0.53	7			90	0.5–1.0	0.65	7
R10	400	mass	15	0.2–0.7/0.8–1.3	0.35/1.12	3/14	CO	15	0.2–0.7/0.8–1.3	0.83/1.35	3/14	
			30	0.5–1.0	0.63	7			30	0.5–1.0	0.71	7
			45	0.5–1.0	0.72	7			45	0.5–1.0	0.79	7
			60	0.5–1.0	0.65	7			60	0.5–1.0	0.76	7
			90	0.5–1.0	0.56	7			90	0.5–1.0	0.70	7

^a N is the number of points in the velocity distribution, which was computed in 1 km s^{−1} bins, used to estimate the slope.

distributions *shallow* slightly over the small length of time simulated here.

- The velocity distributions of H₂ emission for the slow precessing cases contrast with the observationally determined ones, as with our previous simulations. Instead of the observed flat distribution at low velocities, we find a dramatic rise.

5.3 Discussion of position-velocity images and channel maps

In previous papers, we have presented position-velocity (P-V) diagrams in molecular emission lines from various simulations. From simulations of slow precessing jets, we find no additional features and so omit any new figures here.

However, there are some differences. The main one is that in the middle of the projected jet (x') axis, the H₂ diagram appears much less “turbulent”, even in the Q10 pulsed case, than in P10 and thus the flow is much better focussed for the slower precession rate. In the R10 case, the middle portion is contained completely within 0–10 km s^{−1}, although this is not true for the CO emission, which extends out to 20 km s^{−1}.

In R10, rather than the sequence of Hubble Law like P-V regions (that are a consequence of the pulsing) we find an arc of bright material that starts at high velocity (35 km s^{−1}) near the origin and swings down to 10 km s^{−1} near the middle of the plot. About half-way along (from about one-quarter the jet length in x' out to the maximum extent of the jet), the entire range of velocities out to the arc are filled in. In addition, the maximum velocity increases from the middle portion outward, to 25 km s^{−1}.

Analysis of previous velocity channel maps, primarily in CO, revealed a morphological progression as the viewed velocity is changed. High velocity maps show the isolated knotty structures associated with internal shocks along the jet and low velocity maps display the full extent of the shocked ambient medium. In the fast precessing cases, the knots in the high velocity maps are displaced from the mean

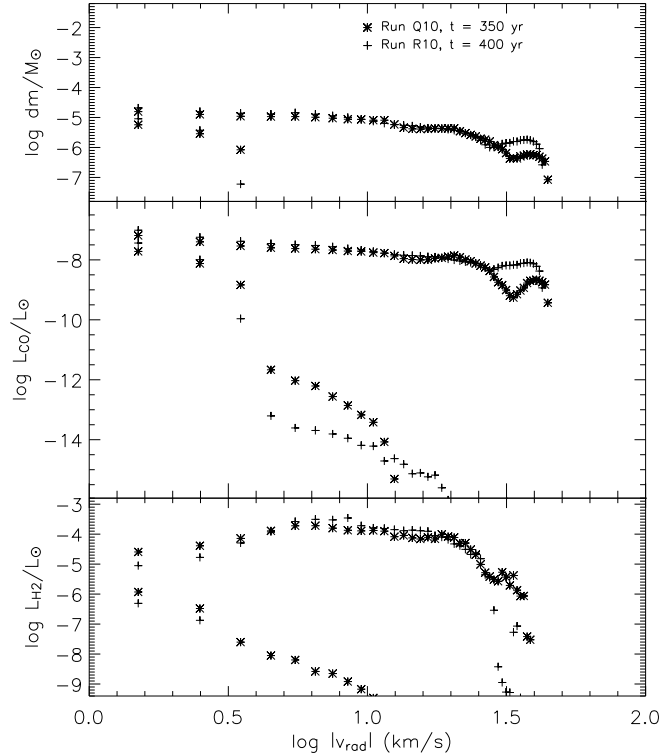


Figure 12. Distribution of velocities into bins of mass and two molecular line luminosities for a viewing angle of 15°. The distributions of mass (top), CO luminosity (middle) and H₂ 1–0 emission (bottom panel) are shown. Each velocity bin is 1 km s^{−1} wide. The designation for the data presented in each panel is shown in the top panel. Each run may be represented twice within each panel, with data from both positive and negative radial velocities included. Naturally, the lower valued data is for the positive radial velocities (which could contribute to a “red” lobe, while the other is from a “blue” lobe).

momentum axis, frequently in an alternating pattern. In the slow precessing, pulsing jet case (Q10), we see a sequence of alternating knots, but the spatial frequency of the oscillation has decreased. In both Q10 and R10, the velocity channel maps indicate that the bright arc within the CO emission near the inlet is at high velocities, while much of the integrated CO emission (Figs. 6 and 8) is at low velocities.

6 SUMMARY OF RESULTS

We have found that the dominant physical structure for all precessing jets is an inward facing cone. In other words, the jet clears out a similar volume of ambient gas. The jaw-shaped structure contrasts with the tube-like structure expected if the jet were to be bent or deflected.

A fast precessing jet generates an impact ring which fairly rapidly disrupts into many mini-bow shocks. Here, slowly precessing jets lead to helical flows that remain noticeably more stable for the duration of the simulation.

A slow precessing and pulsating jet cuts through the ambient medium with the highest speed. We measure this here through an effective drag coefficient. The non-pulsating jet results in a drag coefficient about double that of the pulsating case. Therefore, bow shocks represent the most efficient means of advancing an outflow yet the least efficient at transferring momentum.

The stagnation region at the apex of the inward facing cone displays quite complex time-dependent behaviour in the slow precessing cases. The feature does move slowly forward and accumulates some material, which after some time can be sloughed off to the side open to the ambient medium. We believe that this is the cause for the high transverse velocities measured in these simulations (particularly the non-pulsed R10 case). The feature, which at times can resemble a disk in 3D, is seen in atomic and high energy molecular emission as an “x” feature from certain viewing angles.

The images of molecular emission show quite dramatic evolution. In the pulsed case, the H₂ emission shows a train of asymmetric wedge-shaped bow shocks. The sequence of bow shocks can appear over time to quickly change direction suggesting a violent event at the driving source, yet we are simulating a smoothly varying jet flow. The distribution and structure of the bow shocks appear very similar to the observed HH 240A–D system in the L 1634 outflow (O’Connell et al. 2004). Note, however, that the HH 240 bows have advanced a distance of ~ 0.4 pc from the driving source. Many other groups of bows have been uncovered (e.g. HH 195 and HH 197 5 (Eislöffel 2000)).

On the other hand, shock emission in the form of ribbons is rarely encountered. Examples are HH 222 (Bally et al. 2002), HH 103–105 (Eislöffel 2000) and IRAS 23151+5912 (Weigelt et al. 2005). In fact, HH 222 also possesses an “x” feature, resembling that predicted in our simulations.

The CO cavity patterns found here are largely featureless. In the pulsed case, however, distinct shells may outline the wakes of separated bow shocks which advance directly into the ambient cloud. To observe this property requires resolution and sensitivity which may soon be generally attainable. At present, only one well-known precessing out-

flow, RNO 43, is known to possesses this striking property (Bence et al. 1996).

Many bipolar outflows contain a high fraction of cool gas moving at radial velocities near to that of the embedded cloud. This is derived from CO intensity-velocity relationships which are approximated by a high negative power-law index. In contrast, low power-law indices are associated with these simulations. Hence, the solution to the discrepancy between our results and observations lies elsewhere. It might be reconciled by running the simulations for longer periods of time, which should be easier to perform as faster and larger computing facilities become available. Despite the lack of resolution some interesting outstanding issues, we have shown that the precession rate can dramatically influence the appearance of precessing molecular protostellar jets.

The simulations ignore the effects of the magnetic field. Simulations under ideal magnetohydrodynamic conditions may show significant differences. For example, the magnetic field may stabilise the compressed layer produced by the advancing shock wave. In this case, the fragmentation into multiple bow shocks could be inhibited. In addition, there is mounting evidence that ambipolar diffusion is important in protostellar outflows (Davis 2002; Smith et al. 2003; Giannini et al. 2004). Ion-neutral friction allows the magnetic field to efficiently cushion the shock, spreading and combining the compression and cooling zones. This would have two major effects. Firstly, molecules are not so effectively destroyed until shock speeds approaching 50 km s⁻¹ are reached. Hence, the atomic emission will be even more tightly distributed than here. Secondly, molecular emission is generated from a wider range of shocks. This will tend to increase the length of the wings of bow shocks and the flanks of cavities. Hence, MHD simulations which are directly comparable to those presented in this series should provide more insight.

ACKNOWLEDGMENTS

MDS acknowledges INTAS support through grant 0-51-4838. This research was supported by the Particle Physics and Astronomy Research Council (PPARC) and the Northern Ireland Department of Culture, Arts & Leisure. The numerical calculations were executed on the Armagh SGI Origin 2000 computer (FORGE), acquired through the PPARC JREI initiative with SGI participation, although much of the analysis was performed on a desktop computer acquired through COSMOGRID funding, which also funds AR. As such, some of this work was carried out as part of the CosmoGrid project, funded under the Programme for Research in Third Level Institutions (PRTLI) administered by the Irish Higher Education Authority under the National Development Plan and with partial support from the European Regional Development Fund.

REFERENCES

Arce H. G., Goodman A. A., 2001, ApJ, 554, 132
Bally J., Devine D., 1994, ApJ, 428, L65

Bally J., Devine D., Fesen R. A., Lane A. P., 1995, *ApJ*, 454, 345

Bally J., Heathcote S., Reipurth B., Morse J., Hartigan P., Schwartz R., 2002, *AJ*, 123, 2627

Bence S. J., Richer J. S., Padman R., 1996, *MNRAS*, 279, 866

Beuther H., Schilke P., Gueth F., McCaughrean M., Andersen M., Sridharan T. K., Menten K. M., 2002, *A&A*, 387, 931

Davis C. J., 2002, in *Revista Mexicana de Astronomia y Astrofisica Conference Series H[2]* Observations of Outflows from Young Stars. pp 36–42

Davis C. J., Moriarty-Schieven G., Eislöffel J., Hoare M. G., Ray T. P., 1998, *AJ*, 115, 1118

Dent W. R. F., Matthews H. E., Walther D. M., 1995, *MNRAS*, 277, 193

Downes T. P., Cabrit S., 2003, *A&A*, 403, 135

Downes T. P., Ray T. P., 1999, *A&A*, 345, 977

Draine B. T., Roberge W. G., Dalgarno A., 1983, *ApJ*, 264, 485

Eislöffel J., 2000, *A&A*, 354, 236

Eisloffel J., Smith M. D., Davis C. J., Ray T. P., 1996, *AJ*, 112, 2086

Frank A., Ryu D., Jones T. W., Noriega-Crespo A., 1998, *ApJ*, 494, L79

Giannini T., McCaughrean M., Caratti o Garatti A., Nisini B., Lorenzetti D., Flower D. R., 2004, *A&A*, 419, 999

Gomez M., Kenyon S. J., Whitney B. A., 1997, *AJ*, 114, 265

Gomez M., Whitney B. A., Kenyon S. J., 1997, *AJ*, 114, 1138

Gueth F., Guilloteau S., 1999, *A&A*, 343, 571

Lai D., 2003, *ApJ*, 591, L119

Lee C., Stone J. M., Ostriker E. C., Mundy L. G., 2001, *ApJ*, 557, 429

Lim A. J., 2001, *MNRAS*, 327, 507

Masciadri E., Raga A. C., 2002, *ApJ*, 568, 733

McKee C. F., Storey J. W. V., Watson D. M., Green S., 1982, *ApJ*, 259, 647

O'Connell B., Smith M. D., Davis C. J., Hodapp K. W., Khanzadyan T., Ray T., 2004, *A&A*, 419, 975

Pavlovski G., Smith M. D., Mac Low M., Rosen A., 2002, *MNRAS*, 337, 477

Reipurth B., Bally J., 2001, *ARA&A*, 39, 403

Richer J. S., Shepherd D. S., Cabrit S., Bachiller R., Churchwell E., 2000, *Protostars and Planets IV*, p. 867

Ridge N. A., Moore T. J. T., 2001, *A&A*, 378, 495

Rosen A., Smith M. D., 2003, *MNRAS*, 343, 181

Rosen A., Smith M. D., 2004a, *MNRAS*, 347, 1097

Rosen A., Smith M. D., 2004b, *A&A*, 413, 593

Salas L., Cruz-González I., 2002, *ApJ*, 572, 227

Shepherd D. S., Yu K. C., Bally J., Testi L., 2000, *ApJ*, 535, 833

Smith M. D., 2000, *Irish Astronomical Journal*, 27, 25

Smith M. D., Khanzadyan T., Davis C. J., 2003, *MNRAS*, 339, 524

Smith M. D., Rosen A., 2003, *MNRAS*, 339, 133

Smith M. D., Suttner G., Yorke H. W., 1997, *A&A*, 323, 223

Stanke T., 2000, Ph.D. Thesis

Stone J. M., Norman M. L., 1993, *ApJ*, 413, 210

Sutherland R. S., Dopita M. A., 1993, *ApJS*, 88, 253

Suttner G., Smith M. D., Yorke H. W., Zinnecker H., 1997, *A&A*, 318, 595

Weigelt G., Balega Y., Beuther H., Hofmann K.-H., Preibisch T., Smith M. D., 2005, *A&A*(subm.)

Yu K., Billawala Y., Smith M. D., Bally J., Butner H. M., 2000, *AJ*, 120, 1974